Journal of Solid State Chemistry 183 (2010) 2205–2217

Contents lists available at ScienceDirect

Journal of Solid State Chemistry

journal homepage: www.elsevier.com/locate/jssc

Preparation of $ZnO:CeO_{2-x}$ thin films by AP-MOCVD: Structural and optical properties

A.M. Torres-Huerta [a,*], M.A. Domínguez-Crespo [a], S.B. Brachetti-Sibaja [a], H. Dorantes-Rosales [b], M.A. Hernández-Pérez [b], J.A. Lois-Correa [a]

[a] Instituto Politécnico Nacional, CICATA-Altamira, Km 14.5, Carretera Tampico-Puerto Industrial Altamira, C.P. 89600, Altamira, Tamps, Mexico
[b] Departamento de Metalurgia, Escuela Superior de Ingeniería Química e Industrias Extractivas-IPN C.P. 07300, D. F. México, Mexico

ARTICLE INFO

Article history:
Received 13 May 2010
Received in revised form
20 July 2010
Accepted 22 July 2010
Available online 29 July 2010

Keywords:
$ZnO:CeO_{2-x}$ thin films
AP-MOCVD
Morphology
Structural characterization
Optical properties

ABSTRACT

The growth of columnar CeO_2, ZnO and $ZnO:CeO_{2-x}$ films on quartz and AA6066 aluminum alloy substrates by economic atmospheric pressure metal-organic chemical vapor deposition (AP-MOCVD) is reported. A novel and efficient combination of metal acetylacetonate precursors as well as mild operating conditions were used in the deposition process. The correlation among crystallinity, surface morphology and optical properties of the as-prepared films was analyzed by X-ray diffraction (XRD), scanning electron microscopy (SEM), atomic force microscopy (AFM), transmission electron microscopy (TEM) and UV–vis spectroscopy. The synthesized films showed different crystallographic orientations depending on the ZnO and CeO_2 lattice mismatch, cerium content and growth rate. The CeO_2 films synthesized in this work showed plate-like compact structures as a result of the growth process typical of CVD. Both pure and $ZnO:CeO_{2-x}$ films were obtained with a hexagonal structure and highly preferred orientation with the *c*-axis perpendicular to both substrates under the optimal deposition conditions. The microstructure was modified from dense, short round columns to round structures with cavities ("rose-flower-like" structures) and the typical ZnO morphology by controlling the cerium doping the film and substrate nature. High optical transmittance (> 87%) was observed in the pure ZnO films. As for the $ZnO:CeO_{2-x}$ films, the optical transmission was decreased and the UV absorption increased, which subsequently was affected by an increase in cerium content. This paper assesses the feasibility of using $ZnO:CeO_{2-x}$ thin films as UV-absorbers in industrial applications.

1. Introduction

Zinc oxide (ZnO) is an important and promising material with many typical properties such as transparency in the visible range, direct band gap of 3.3 eV, electrochemical stability, semiconductor resistivity (10^{-3}–10^5 ohm-cm) and non-toxicity [1,2]. The interest in low dimensional nanostructured particles and thin ZnO films has been significantly increased in recent years, with the realization of devices such as LED [3], UV laser [4], solar cells [5] and sensors [6]. On the other hand, nanocrystalline ceria (CeO_2) particles and ceria doped films have recently been extensively studied because of their very interesting properties that are especially suitable for technological applications such as energy storage [7,8] and catalysts [9–11] due to the capacity of these materials for storing or releasing oxygen. Additionally, CeO_2 has been used as a protective coating against corrosion [12], and applications in many different fields have been found from ceramics, coatings and sensors to biomaterials and cosmetics [13]. The controlled synthesis and properties of ZnO nanostructures grown by different techniques has been widely reported; however, the effects of rare earth doping for practical applications has been rarely stated [14]. In addition, it is well known that the synthesis of technologically useful materials depends not only on the quality of the crystal and surface chemistry, but also on the spatial orientation and arrangement [15]. Then, it is expected that by co-deposition of $ZnO:CeO_{2-x}$ some properties such as UV absorption, controlled band gap, photoluminescence, extinction coefficient, anticorrosive properties and refractive index can be improved by cerium inner shell transitions [14,16]. In recent years, various kinds of ZnO and CeO_2 nanostructured thin films have been successfully synthesized, but high density and well ordered nanostructures are needed for practical applications [17–19]. These structures can be synthesized by a variety of techniques such as sputtering, reactive thermal evaporation, chemical spray technique, pulsed laser deposition, metal-organic vapor deposition (MOCVD), electrochemical impregnation and sol–gel [18,20–25]. In comparison with other techniques, MOCVD has several advantages, including fine control of the partial pressure of individual reactants, thickness, well ordered structures with highly uniform areas and high growth rate (in contrast

* Corresponding author.
E-mail addresses: atohuer@hotmail.com, atorresh@ipn.mx (A.M. Torres-Huerta).

0022-4596/$ - see front matter © 2010 Elsevier Inc. All rights reserved.
doi:10.1016/j.jssc.2010.07.037

with MBE, PLD, etc.), which could facilitate the reproducibility and controlled synthesis of high quality thin films [26,27]. Although, the synthesis of ZnO can be done by means of the useful MOCVD technique, its production from zinc metal-organic materials such as diethyl-zinc or dimethylzinc is inconvenient because these starting compounds can react violently with air or water even at low temperatures; and besides, the high cost of these precursors makes more difficult the synthesis of this compound. The aim of this work is to analyze the effect of adding a rare earth element (16:9, 18:6 and 20:3 metallic ratio; 10, 20 and 30 wt% of cerium precursor) on the structure, morphology and optical properties of ZnO thin films using MOCVD at atmospheric pressure, which have been rarely reported. Therefore, the trials were performed on NaCl monocrystals (111) and quartz. A metallic substrate was also analyzed on order to analyze the structural properties on polycrystalline substrates and afterwards to propose them as possible anticorrosive coatings. For comparison purposes, APMOCVD (atmospheric pressure MOCVD) was also used to grow pure films of both ZnO and CeO_2. X-ray diffraction patterns, XRD, atomic force microscopy, AFM, scanning electron microscopy, SEM, transmission electron microscopy, TEM, and UV–vis were used to perform the structure, topography, morphology, crystallite size and optical characterization.

2. Experimental section

2.1. Substrates

In this work, three types of substrates were used; polished quartz ($45 \times 25 \times 1$ mm^3), NaCl monocrystals (111) and commercial AA6066 aluminum alloy ($30 \times 30 \times 3$ mm^3) plates. Before the APCVD process, the metal surface was mechanically ground starting from 120- to fine 1500-grade emery papers, according to the ASTM standard [28], while the quartz substrates were cleaned with a soapy solution, and thereafter rinsed with tap water, deionized water and acetone.

2.2. Precursors

The precursor choice was made by taking into account the low volatility inherent to some β-diketonate precursors, low melting temperature, decomposition temperature and high vapor pressure. Most oxide depositions are achieved at reduced pressures, ranging from just a few torr to ten torr. Atmospheric vapor deposition becomes feasible when the precursor is sufficiently volatile. Then, a volatile precursor and chemical stability play an important role in the deposition parameters. It is the case of zinc and cerium acetylacetonates. Additionally, the precursor compound should permit at least one reaction mechanism through which a clean deposition reaction with little contamination can be carried out. For these reasons, the selected precursors were zinc acetylacetonate hydrate [$Zn(C_5H_7O_2)_2 \cdot xH_2O$, Fluka, $\geq 90\%$] and cerium acetylacetonate [$Ce(C_5H_7O_2)_3 \cdot xH_2O$, Sigma Aldrich, $\geq 90\%$].

2.3. MOCVD Experiments

All the film depositions were carried out in the original setup made from tubular quartz consisting of a three-zone-hot-wall-gas-flow reactor (120 in length and 5 cm in diameter) under atmospheric pressure. ZnO and CeO_2 films were obtained in order to find the growth conditions of the ZnO:CeO_{2-x} coatings. For ZnO:CeO_{2-x} films, different ratios of $Zn(acac)_2$ and $Ce(acac)_3$ (70:30, 80:20 and 90:10 wt% corresponding to 16:9, 18:6 and 20:3 ratios of Zn/Ce metallic base, respectively) were placed in a quartz boat and hand mixed. Afterwards, the quartz boat was introduced into the CVD reactor under argon and oxygen atmosphere using a flow rate of 100 cm^3 min^{-1}. The vapors were conducted into the hot zone maintained at temperatures ranging from 400 to 700 °C.

2.4. Characterization of the precursors

It is known that Zn $(acac)_2$ melts at 136–138 °C, but there is no information for $Ce(acac)_2$; thus thermogravimetric and calorimetric analyses (TGA/DSC, in a SDT-Q600) were carried out in order to determine the melting and decomposition points of both precursors using a heating ramp of 10° min^{-1}.

2.5. Film characterization

The phase composition and crystal structures of the as-synthesized films were determined by powder X-ray diffraction using a Bruker D8 Advanced, Cu K_α radiation at 35 kV, 25 mA and a scan rate of 0.02° min^{-1}.

The morphology, estimated thickness and surface roughness of the film were examined by scanning electron microscopy using a SEM JEOL JSM 5600 LV and JSM 6300; atomic force microscopy by

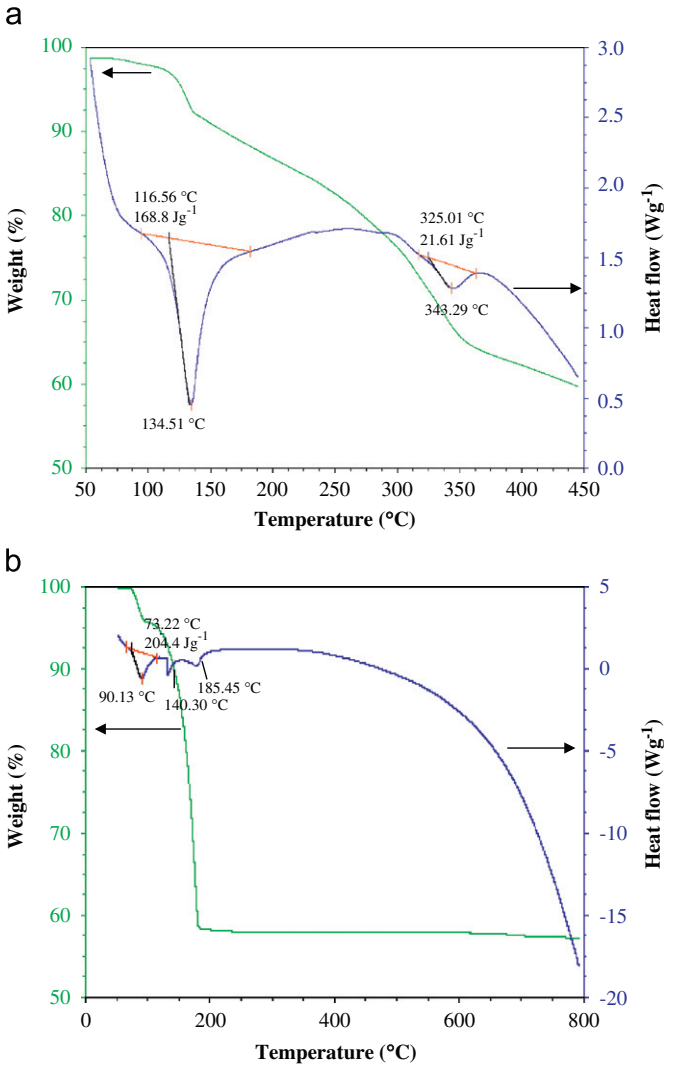

Fig. 1. TGA/DSC curves of (a) $Ce(acac)_3$ and (b) $Zn(acac)_2$. Heating rate: 10 K/min in helium atmosphere.

AFM, Nanosurf easyscan 2 AFM/STM in contact mode with a Si cantilever and nominal force of 20 nN, respectively.

The phase composition and structure of the films were also analyzed by transmission electron microscopy using a JEOL-2000 FX-II. During the TEM measurements, the as-prepared films were deposited onto a NaCl monocrystal (111).

The optical transmittance measurement of these films was carried out using an UV–vis spectrometer Lambda 40 Perkin Elmer within the range of 200–1100 nm.

3. Results and discussion

3.1. Characterization of the precursors

Fig. 1a and b reports the TGA/DSC scan performed on commercial (a) $Ce(acac)_3$ and (b) $Zn(acac)_2$ precursors. For $Ce(acac)_3$, a weight loss of ~8% at 116.56 °C is observed due to the dehydration followed by a second slow loss that occurs around 325.01 °C; it represents up to 27.22% of the weight of the precursor. DSC analysis confirms that the decomposition occurs in two steps. The first endothermic peak centered at 134.51 °C corresponds to the first weight loss shown by TGA and is ascribed to the dehydration. The second endothermic peak at 343.29 °C can be ascribed to the melting point of $Ce(acac)_3$. On the other hand, the TGA and DSC curves for $Zn(acac)_2$ displayed an endothermic peak around 90.13 °C, which is associated with the water molecule evaporation that caused 10% of the weight loss. Endothermic peaks at about 140.30 and 185.45 °C were clearly observed, which are possibly related to the melting point and the total decomposition of the precursor, respectively. The regular endothermic reaction starting from 186 °C is due to the slow kinetics of the thermolysis reaction in He.

Depending on the conditions, there are several decomposition routes of metal acetylacetonates. According to Fig. 1a and b, the decomposition process of $Ce(acac)_3$ and $Zn(acac)_2$ in inert gas already starts at 325.01 and 140.30 °C, respectively; $Ce(acac)_3$ and $Zn(acac)_2$ are not the only volatile species responsible for the ZnO formation in MOCVD. However, taking into account all the precursor destruction paths is a difficult task [29], it is common to use an overall CVD reaction. In this case, the possible chemical reactions that take place are:

$$6Ce(C_5H_7O_2)_3 \cdot xH_2O + 109O_2 \rightarrow 4CeO_2\downarrow + Ce_2O_3\downarrow + 90CO_2\uparrow + 69x\ H_2O\uparrow \quad (1)$$

$$Zn(C_5H_7O_2)_2 \cdot xH_2O + 12O_2 \rightarrow ZnO\downarrow + 10CO_2\uparrow + 8x\ H_2O\uparrow \quad (2)$$

From the TGA/DSC results, the CVD experimental conditions were determined and reported in Table 1. The precursor temperatures were adjusted due to differences in their melting points, considering that in the mixture the major quantity corresponds to ZnO.

Table 1
AP-MOCVD deposition parameters for the as-deposited films.

Thin film	Precursor temperature (°C)	Deposition temperature (°C)	Gas flow, argon ($cm^3\ min^{-1}$)	Gas flow, oxygen ($cm^3\ min^{-1}$)	Weight of precursor (mg)
CeO_2					100
ZnO					100
ZnO:CeO_2 (20:3)	130	400–700	100	100	90:10
ZnO:CeO_2 (18:6)					80:20
ZnO:CeO_2 (16:9)					70:30

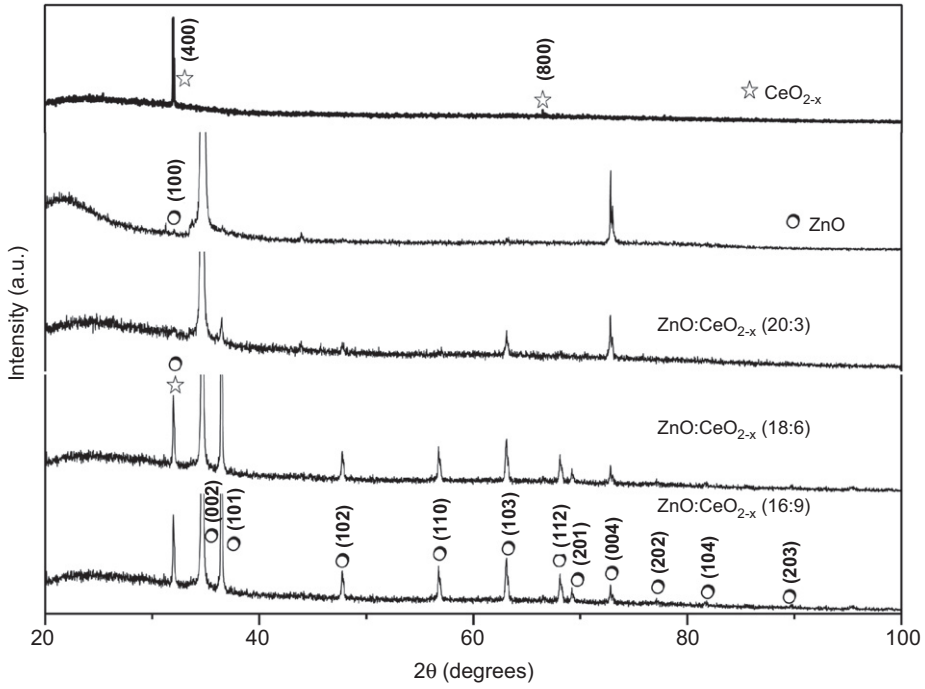

Fig. 2. XRD diffractograms of CeO_2, ZnO and ZnO:CeO_{2-x} films on quartz substrates.

3.2. Film compositions and structural characterization

All the as-deposited films only contained Zn and Ce oxides. DRX and EDS did not reveal any detectable amount of carbon or metals other than ZnO and CeO_{2-x} in the films.

Due to CeO_{2-x}, ZnO compounds and rare earth doping ZnO thin films have been widely used as an active component in three-way catalysts for automobile exhaust gas treatment, UV blocking filters, electrochromic displays and optical devices [14,30–33], the structure of the crystal lattice and atomic arrangement for stoichiometric and non-stoichiometric compounds are extremely important to understand their effects on mechanical, electrochemical and optical properties. Fig. 2 shows the XRD patterns of the as-prepared CeO_{2-x}, ZnO and ZnO:CeO_{2-x} films on

Table 2
Lattice parameters.

Lattice parameters	CeO_{2-x}	ZnO	ZnO:CeO_{2-x} (20:3)	ZnO:CeO_{2-x} (18:6)	ZnO:CeO_{2-x} (16:9)
a (Å)	5.815	3.226	3.227	3.244	3.244
c (Å)	–	5.188	5.193	5.186	5.187
c/a	–	1.608	1.609	1.598	1.598
u	–	0.3808	0.3806	0.3832	0.3832

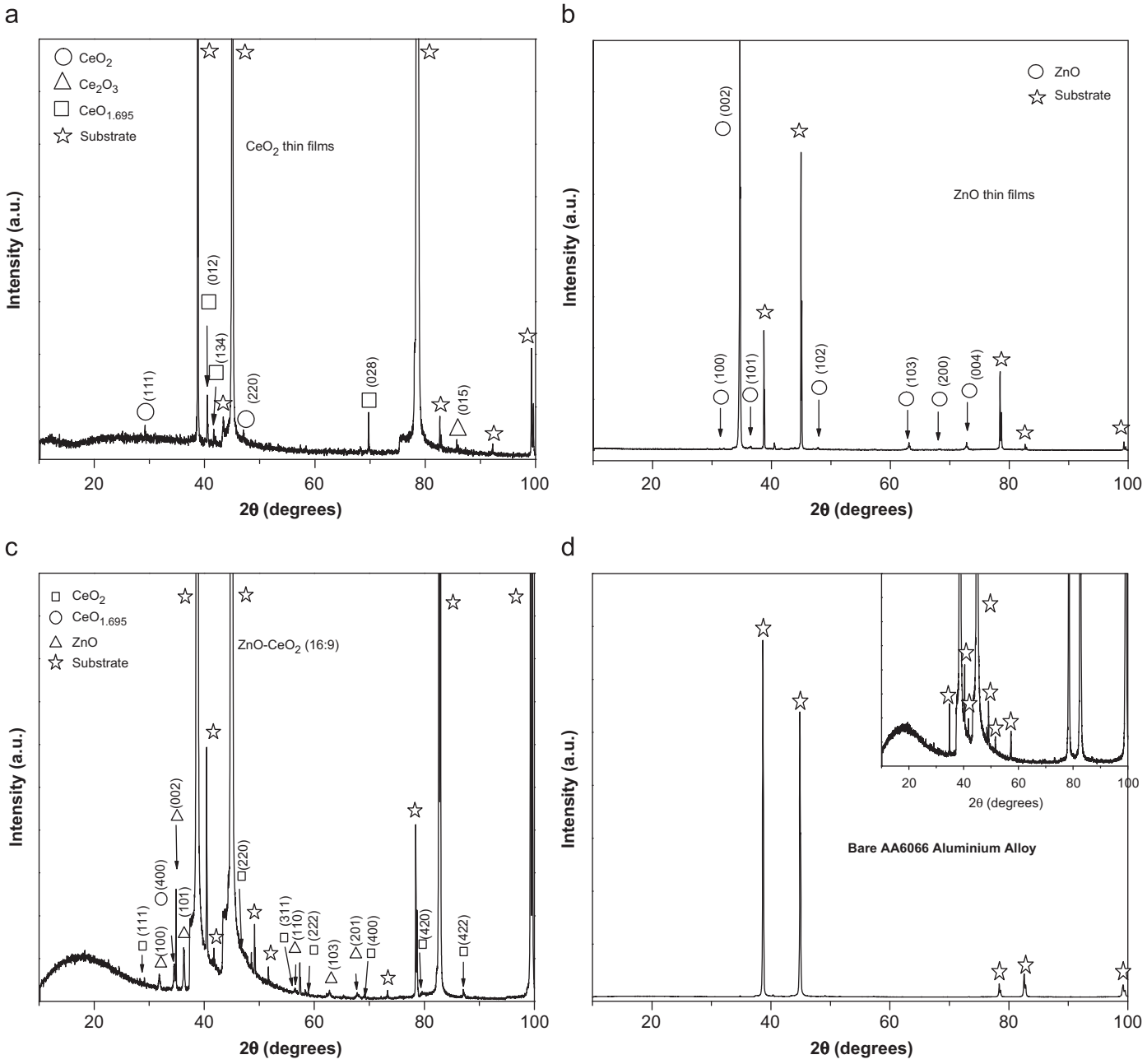

Fig. 3. XRD diffractograms of (a) CeO_2, (b) ZnO, (c) doped ZnO thin films with a metallic 16:9 ratio on AA6066 substrates and (d) metallic substrate.

quartz. Cerium oxides in the form of CeO_{2-x}, with $x=0.305$ were detected during XRD measurements on quartz substrates (Fig. 2). The CeO_{2-x} films are mainly crystallographic oriented towards the (4 0 0) plane, although, it is also observed, with low intensity, the (8 0 0) plane. Stoichiometric CeO_2 has a cubic fluorite (CaF_2) with a lattice constant of 0.541 nm and a band gap of ca. 6 eV [34].

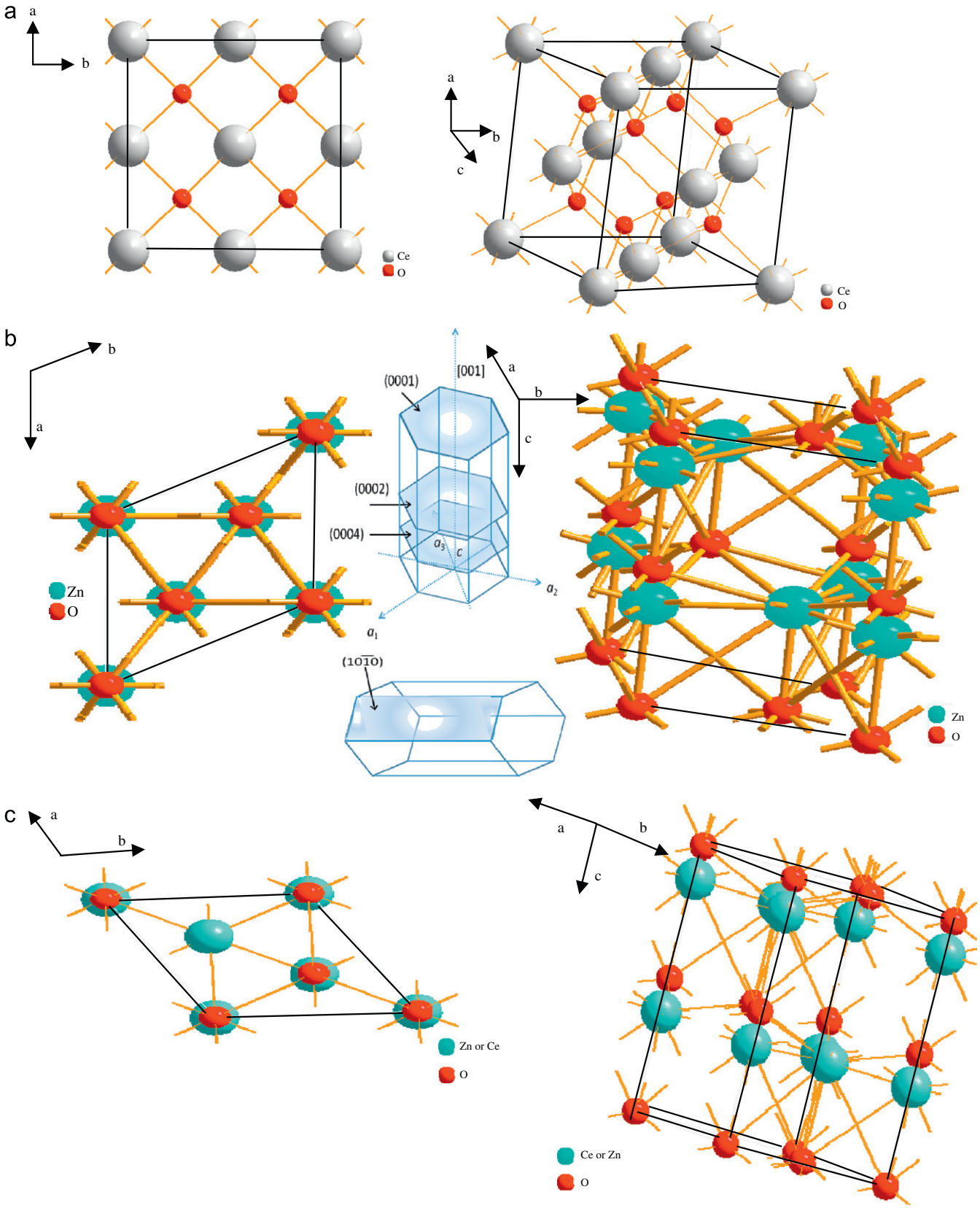

Fig. 4. Schematic representation of unit cell (a) CeO_{2-x}, (b) ZnO and (c) ZnO:CeO_{2-x} with the representation of main out-of plane orientations for as-growth films on the substrates.

Nevertheless, the lattice parameters calculated by the UnitCell Software [35] for the as-prepared CeO_{2-x} films indicate a mismatch in the lattice constant of 0.040 nm (Table 2). The differences can be explained in terms of the structural change; while stoichiometric CeO_2 displayed an fcc structure, the $CeO_{1.695}$ showed a bcc structure. On the other hand, pure ZnO films displayed the typical hexagonal wurzite structure which grows on a preferential plane (0 0 2). From XRD patterns, it is clear the influence of CeO_2 on the number of detected signals from ZnO; i.e. the polycrystalinity increased as the cerium quantity increases.

Recently, we reported no diffraction peaks arising from CeO_{2-x} compounds or other impurity phases in the ZnO:CeO_{2-x} thin film spectra [36]; however, a more detailed analysis in the as-deposited samples indicated that a non-stoichiometric CeO_{2-x} could be present during the growth of the films, and the first signal is the result of the contribution of both materials (ZnO:CeO_{2-x}) in the hexagonal structure.

In comparison with the JCPDS 36-1451, $a=3.249$, $c=5.206$ Å chart, the lattice parameters for the as-synthesized samples (Table 2) showed a mismatch of lattice constant that can be correlated with the internal strain during film formation and the partial interstitial substitution of the Ce^{4+} ion provoking the reduction of the lattice constant. Similar results have been reported by Yang et al. [37] who suggested that cerium ions would uniformly substitute into the Zn^{2+} sites or interstitial sites in the ZnO lattice. ZnO is a polar crystal whose polar axis is the *c*-axis, and its space group is $C_6^4=p6_3mc$. In this structure, each Zn^{2+} ion is surrounded by four O^{-2} ions and vice versa [38]. Hence, the close correlation between the c/a ratio and u (length of the bond parallel to the *c*-axis) parameter can be explained as follows: when the c/a ratio decreases, the u parameter increases in such a way that the four tetrahedral distances remain nearly constant through a distortion of tetrahedral angles due to long-range polar interactions [39]. The obtained c/a ratios and preferential growth ZnO films with and without cerium are in good agreement with results reported elsewhere [38–40].

Fig. 3 shows XRD patterns of CeO_2, ZnO and ZnO:CeO_{2-x} thin films grown on AA6066 aluminum alloy. For comparison purposes, the response of the substrate after mechanical polishing was also displayed in Fig. 3d. The XRD patterns for CeO_2 (Fig. 3a) exhibit different species of cerium oxides that correspond to Ce (III), Ce (IV) and non-stoichiometric oxide

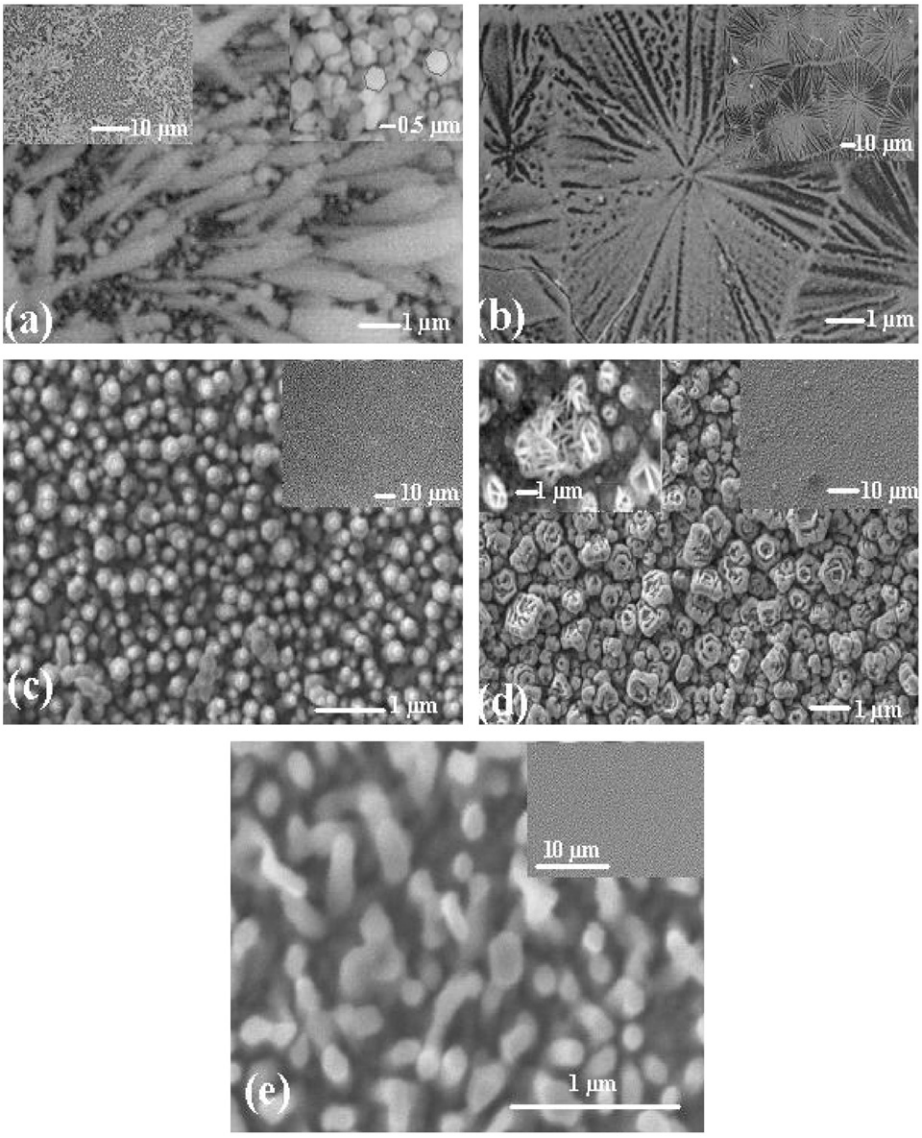

Fig. 5. SEM micrographs of the as-deposited films on quartz (a) ZnO, (b) CeO_{2-x}, (c) ZnO:CeO_{2-x} (20:3), (d) ZnO:CeO_{2-x} (18:6) and (e) ZnO:CeO_{2-x} (16:9). The inset figures show low magnifications of the surface coatings.

($CeO_{1.695}$), which can be explained in terms of the reaction (1). Oxygen deficiencies led the reduction of Ce^{4+} to Ce^{3+} and to the occupation of the empty states left in the band gap, which also could explain the formation of the third oxide ($CeO_{1.695}$) [30]. Probably due to the film thickness, in the XRD measurements, signals arising from the metallic substrate can also be observed. The ZnO film grown onto the metallic substrate did not show changes in the typical hexagonal wurzite structure (Fig. 3b), and it preferentially grew on the (002) plane. Interestingly, the co-deposited ZnO:CeO_{2-x} thin films on AA6066 aluminum (Fig. 3c) only displayed a combination of CeO_2 and non-stoichiometric compounds, but the Ce_2O_3 signals are missing. Apparently, the ZnO structure is playing an important role in the oxygen deficiencies provoking the predominance of non-stoichiometric CeO_{2-x} species.

The observed differences in both substrates show that the amorphous substrate favors the non-stoichiometric $CeO_{1.695}$ with a (400) crystallographic orientation, whereas the crystalline substrate induces the formation of a mixture of cerium oxides forming the polycrystalline films. A schematic representation of the growth films is shown in Fig. 4a–c. It should be noted that cerium atom is substituting some Zn positions which deforms the lattice as shown in Table 2.

It is well known that, theoretically, the (111) surface is the most stable surface among the low index planes [41,42]; however, direct observations of the AP-MOCVD structures obtained here, showed that the other low index planes and formation of cerium oxide compounds can be produced by controlling the deposition parameters and substrate. Additionally, the films are textured, i.e. there are preferred orientations, then, some reflections are anomalously intense, and there are changes in the relative intensities of the reflections in comparison with those obtained with a randomly powdered specimen (JCPDS charts). The presence of texture is common in materials such as films, and in this case, the reflections missing in the film diffraction patterns, are missing not because they are forbidden by the structure factor, but because the grains are no oriented in the correct way to allow diffraction to occur from these planes.

3.3. Morphological characterization

The morphology of transparent CeO_{2-x}, ZnO and ZnO:CeO_{2-x} films on both quartz and aluminum substrates are shown in Figs. 5–7, respectively. The morphology of ZnO films displays randomly aligned ZnO columns on the quartz substrate under the growth conditions (Fig. 5a). These results show that the columns cover uniformly the surface substrate, but the length of the columns is irregular (inset figure); this length is changing from several hundred nanometers to some micrometers ($\sim$2.1 μm). The thickness of these films was about 2.1 μm with a deposition rate of 17 nm min^{-1} (Fig. 6a). The grown crystals belong to the hexagonal crystal system, with a mean diameter of about 300 nm. The CeO_{2-x} thin films show grain boundaries with an apparently distorted five-fold shape (inset in Fig. 5b) that is clearly observed; these grains grow as radial-like dendrites with a great size (approx. 70 μm × 50 μm); these films are compact, dense and cover uniformly the substrate surface. Small cracks caused by tensile stress are also observed in some regions of the CeO_{2-x} thin films. According to Al-Kuhaili et al. [43], CeO_2 thin films have a columnar microstructure, and therefore, are highly porous. Porosity arises because of the presence of voids in the columnar microstructures, and these voids provide direct access to the molecules flowing in from the environment, but the CeO_{2-x} films synthesized in this work show a plate-like compact structure product of the growth process typical of CVD [44] with a thickness

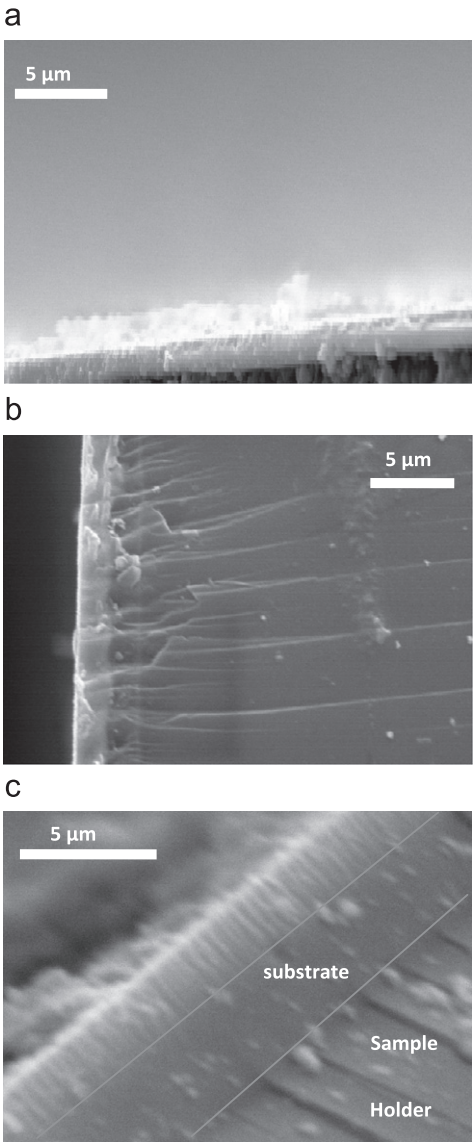

Fig. 6. The cross section SEM micrographs of the as-deposited films, (a) aligned ZnO columns on the quartz substrate, (b) plate-like compact CeO_2 structure product and (c) ZnO–CeO_{2-x} (20:3) with the typical ZnO growth.

of about 2.3 μm (Fig. 6b). The morphology of the as-grown ZnO:CeO_{2-x} films is shown in Fig. 5c–e. From the SEM observations, it is clear that the coatings are well formed on the quartz substrates (inset figures); however, important changes in the morphology and shape of the crystals forming the films such as cerium content increase are pointed out. Hence, the microstructure is modified from dense, short round columns (Fig. 5e) to round structures with cavities ("rose-flower-like" structures, Fig. 5d), and the hexagonal form is detected indicating the typical wurzita ZnO. Finally, at low cerium content (Fig. 5c), the film changes to the typical ZnO morphology, i.e. hexagonal columns described as the ideal growth habit of ZnO crystals [38]. The film thickness in this system is about 2–2.4 μm with deposition rates ranging from 17 to 20 nm min^{-1} (Fig. 6c). The observed microstructure and XRD results can be explained in terms of the mismatch between the fcc CeO_2 and hexagonal ZnO, and the different growth mechanisms i.e. apparently, CeO_{2-x} is inhibiting the growth of hexagonal ZnO columns when present in high quantity. Although the XRD measurements showed the presence of cerium and zinc oxides, suggesting two phases

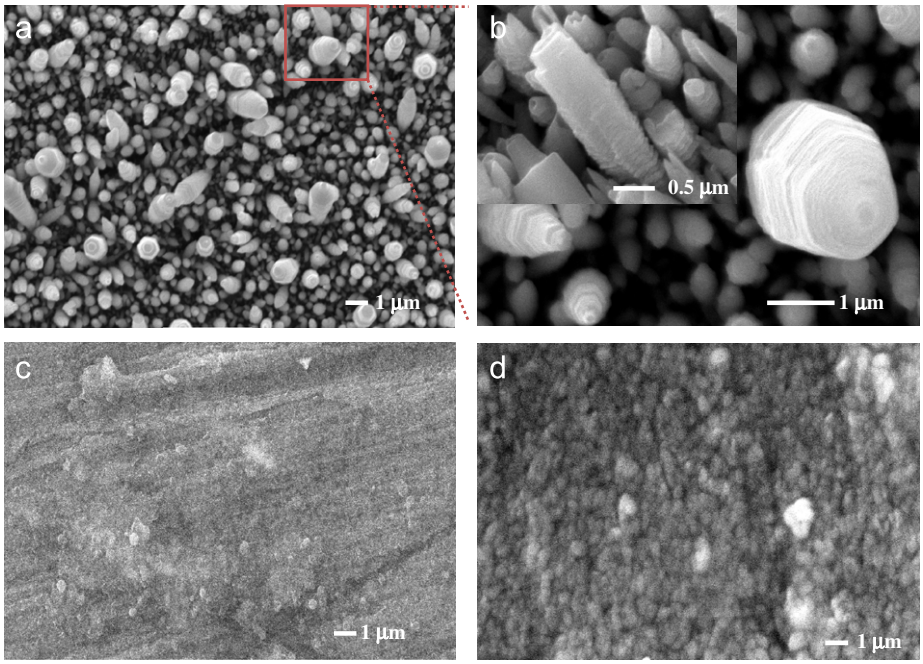

Fig. 7. SEM micrographs of the as-synthesized films on metallic substrates, (a–b) ZnO at different magnifications, (c) CeO_{2-x} and (d) ZnO:CeO_{2-x} (16:9). The inset figure in (b) shows the enlarged image of the selected area of the columns showing the crystal growth.

forming the film, the SEM micrographs only showed one phase. Therefore, when CeO_{2-x} is present in a low content, it is incorporated into the ZnO lattice allowing the development of hexagonal columns as it has been suggested by Yang et al. [37], whereas with high cerium contents, a strong lattice deformation is observed, which modified the typical crystal growth.

ZnO thin films pure and with a higher cerium quantity deposited on metallic substrate are shown in Fig. 7a–d. This figure also shows the CeO_{2-x} as-deposited films. The characteristic ZnO hexagonal columns are again observed in the micrograph (Fig. 7a and b), but in this sample, the crystals are better oriented over the substrate than those observed in the quartz substrates. The columnar arrangement in this case displayed different sizes ranging from several hundreds of nanometers to 2.5 μm. From these results, it is clear that the synthesis process can be described as a successive stacking of entities constructed from layers respectively made of O and Zn atoms [24,45]. The anisotropy of the crystals is related to the growth rate, which is higher along the *c*-axis for ZnO during the synthesis. The cerium oxide film deposited on AA6066 aluminum alloy substrates displayed a smooth surface composed of very fine grains whose thickness is about 2.2 μm yielding a growth rate of about 18 nm min^{-1}. The surface of these samples is crack-free, dense and compact, but with a quite different structure from that observed on the quartz substrates. Finally, the ZnO:CeO_{2-x} thin films (16:9 metallic ratio) did not show clearly the typical wurzite structure with grain shape-like-semispherical nanorod. It must be noted that the bottom and top diameters of these crystals are uniform with an average value of 200 nm. The shapes of these columns are again different to the observed morphology in the as-prepared samples on quartz; however, in this case, the traditional flower-like nanorod clusters frequently attributed to the agglomerated ZnO nuclei in the initial stage cannot be observed [46]. Ce may be an ideal material to be doped or added into ZnO nanorods due to the similar lattice constant. So, a possible mechanism for the other deposition technique of ceria doped ZnO nanorods at a similar temperature has been proposed. This was ascribed to a preferential transformation of Ce^{3+} ions. It is well known that an impetus for aggregation of nanoparticles is to reduce surface energy by eliminating the highest energy surface [47]. Some of the crystal faces could well reduce the surface energy of ZnO, and nanocrystalinity can be quickly formed under our deposition conditions; however, further analyses are required in order to determine the interactions between ZnO:CeO_{2-x} and cerium oxidation state. In addition, the grain size will depend on the surface and grain boundary energies. If the grain boundary energy is independent of the texture, the deposit in which a smaller surface energy plane is placed parallel to the substrate is expected to have larger grains in order to reduce the film energy; on the contrary, if the grain boundary energy is dependent on the texture, shorter grains could be obtained. Then the fine grains observed with higher cerium content could also be due to the film texture.

Fig. 8a–e shows the atomic force microscopy of the as-grown films with and without cerium at different metallic ratios 16:9, 18:6 and 20:3. These micrographs correspond to the topography and three-dimensional images of the samples using SPIP 4.80 and Nanosurf easy scan 2.0 software. The results are in good agreement with SEM observations with a uniform and dense morphology. From these results, it is corroborated that the particle sizes ranged from 100 nm to 2 μm in diameter as a result of nucleation and coalescence mechanism during the growth process. The rms average surface roughness (R_a) and mean square of the Z data (R_q) values of the CeO_{2-x}, ZnO and ZnO:CeO_{2-x} thin films are shown in Table 3. In this case, the Z value is defined as the difference between the highest and lowest points within the given area. The and CeO_{2-x} displayed a smoother surface than that observed for those ZnO and ZnO:CeO_{2-x} films.

According to Al-Kuhaili et al. [43], CeO_2 thin films have columnar microstructure, and therefore, they are highly porous. Porosity arises from the presence of voids in the columnar microstructure, and these voids provide direct access to the molecules flowing from the environment; but the CeO_{2-x} films synthesized in this work show a plate-like compact structure (Fig. 8a), product of the growth process typical of CVD [44].

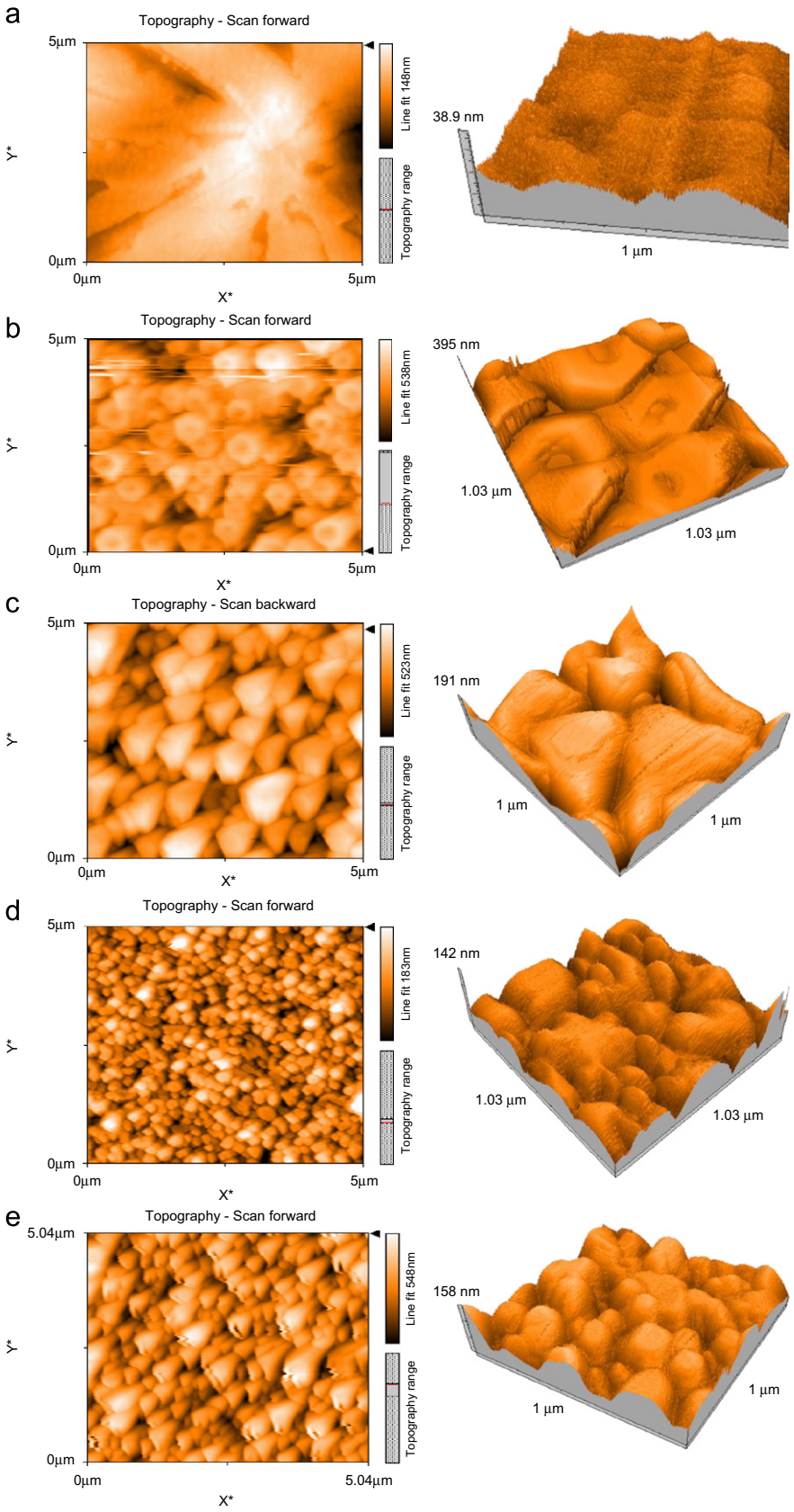

Fig. 8. AFM images of (a) CeO_2, (b) ZnO and (c–e) $ZnO:CeO_{2-x}$ films at 20:3, 18:6 and 16:9 metallic ratios, respectively.

On the other hand, both parameters, R_a and R_q of the $ZnO:CeO_{2-x}$ films, are also in agreement with the SEM observations because the coating corresponding to 18:9 wt% of Zn and Ce metallic base presents a higher number of cavities that increased the roughness values, while the $ZnO:CeO_{2-x}$ (16:3) displayed a smoother surface than the other films. Then, as cerium quantity

Table 3
Roughness data of ZnO–CeO_2 from AFM images.

Roughness	CeO_2	ZnO	ZnO–CeO_2 (20:3)	ZnO–CeO_2 (18:6)	ZnO–CeO_2 (16:9)
R_a (nm)	3.999	43.415	49.201	41.052	15.792
R_q (nm)	5.0735	57.58	62.272	50.273	19.967

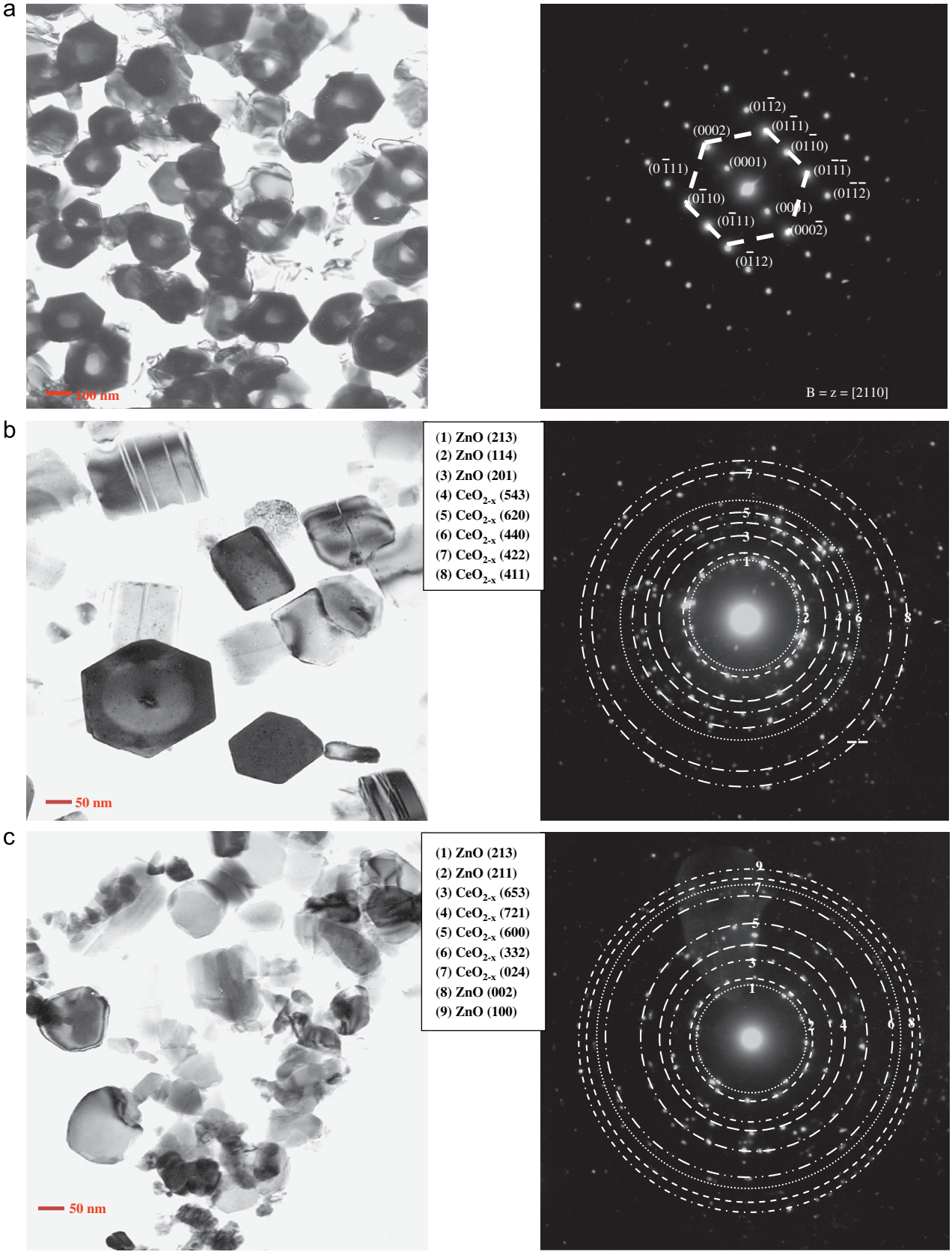

Fig. 9. TEM micrographs and their corresponding SAED pattern obtained for the as-deposited thin films for (a) ZnO, (b) ZnO–CeO_{2-x} (20:3) and (c) ZnO–CeO_{2-x} (16:9).

increases the tensile strain in the lattice, the surface roughness and polycrystallinity of the films are also increased as the XRD analyses showed.

The structure of the as-grown films in selected samples was also analyzed by TEM and selected area electron diffraction patterns (SAED). Fig. 9a–c clearly shows the evolution of the particle shape due to the integration of cerium into the ZnO wurzite structure (from hexagonal to irregular shapes), which is more evident when the cerium concentration is increased. The SAED patterns obtained for the ZnO (Fig. 9a) presented spot transmission diffraction patterns that correspond to the hexagonal structure of the micrometric order, where all the ZnO:CeO_{2-x} films show a SAED pattern with circular sections instead of the completed ring characteristics of disoriented crystals, thus revealing the variety of the particle sizes forming the film. The SAED patterns of the ZnO:CeO_{2-x} deposited films confirm the (002) and (101) and (004) planes are in agreement with the XRD results, suggesting a good *c*-axis alignment to the growth direction. Furthermore, other planes are detected, corroborating the strong influence of the substrate on the grown films. These results are in good agreement with the prediction (for hcp structures) of the preferred growth model in which a good *c*-axis alignment to the growth direction is favored at relatively low deposition temperatures [48]. It is well known that the growth temperature strongly affects the diameter and aspects ratio of the columns; then, at the deposition temperature of this work (~500 °C), the mean diameter of the rod varies from several hundred nanometers to several micrometers.

3.4. Optical properties

The optical properties were investigated by spectroscopic measurements. Optical absorbance and transmittance spectra of all the films deposited on glass substrate were recorded in the wavelength range from 200 to 1100 nm using a Perkin Elmer double beam spectrometer. The typical absorbance and transmittance curves for the obtained films are shown in Fig. 10a and b. The influence of added cerium content in the ZnO films is clearly observed on the absorbance and transmittance properties. The ZnO:CeO_{2-x} films have high absorption in the UV and visible regions followed by a steep fall-off in the absorption at approximately >400 nm (Fig. 10a), whereas pure ZnO films have lower absorbance in visible region. This behavior may be due to the introduction of CeO_{2-x} defective states within the forbidden band, which may lead to absorption of incident photons. The edge of ZnO:CeO_{2-x} films appeared to shift towards the lower wavelength side. The two main transitions involved in the absorption of CeO_{2-x} films in the vis–UV range may explain this behavior: from the highest occupied valence 2*p* oxygen band into empty 4*f* states of cerium at approximately 4 eV (O2*p*→Ce4*f*), and from the *sp*-band into the *d* conduction band at approximately 9 eV (O2*p*→Ce5*d*) [31].

It is also observed that the pure ZnO film is the most transparent one (>87%), and transparency decreases up to 74.18% with higher cerium concentration, and 73.94% for CeO_{2-x} films in the visible region (Fig. 10b). The transparency of ZnO at 1098 nm, which is the laser excitation wavelength, makes it a good candidate for nonlinear optical applications, and it is comparable with other deposition techniques [14,49]. On the other hand, the most important percentage of transparency for ZnO:CeO_{2-x} films is obtained with a low cerium concentration (80.85%), corroborating the observed morphology; the results are not better than pure ZnO films. Then, cerium doping did not improve the transparence in the visible region, but it increased

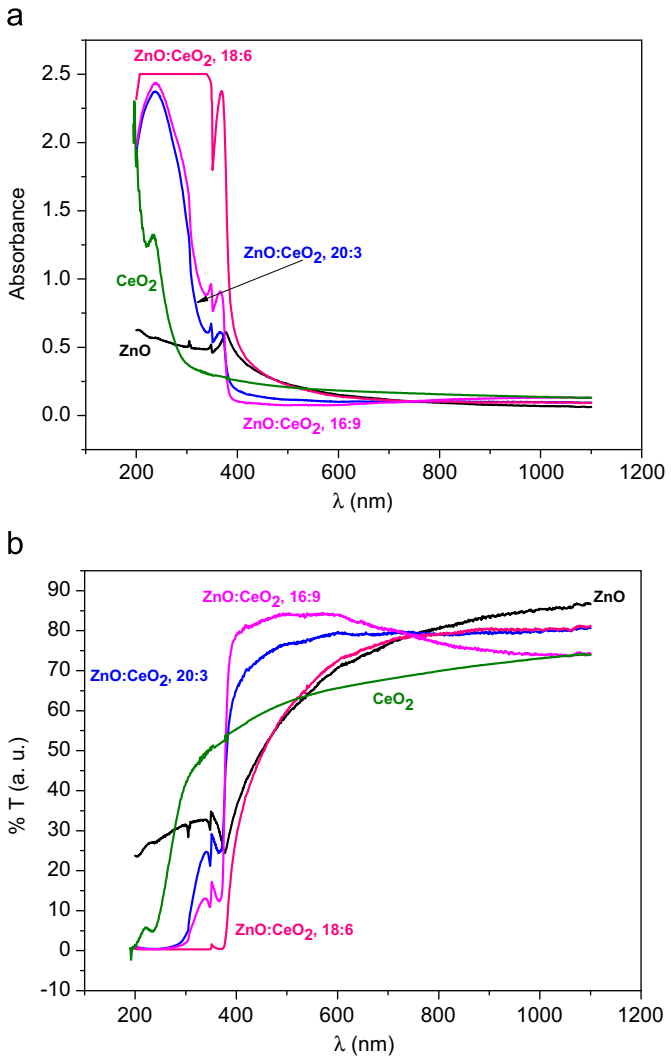

Fig. 10. The (a) absorbance and (b) transmittance spectra of the as-deposited films.

the absorption in the UV region, which makes it suitable as an UV absorber (protecting light-sensitive materials) [50].

From the optical absorption theory of direct transition in semiconductors, the relation of the band gap E_g, the incident photon energy $h\nu$, and the transmittance T, can be expressed as follows [1]:

$$\ln^2 T = C(h\nu - E_g) \quad (3)$$

Considering that C is a constant, the band gap can be obtained by a linear fitting as shown in Fig. 11. The calculation of the band gap from fitting is also shown in Table 4. The values calculated from the absorption data indicated that the gap energies for ZnO films are around 3.75, 3.25 and 2.22 eV. The band gap for this film is usually found at 3.3 eV; then, the significant differences of E_g can be due to the different lengths obtained in the rods, which also cause differences in the film thickness. This behavior is frequently related to a film with different grain sizes [51,52]. On the other hand, the values of the optical band gap for CeO_{2-x} films are about 4.06–5.18 eV. These values are higher than the band gap values reported on fully oxidized CeO_2 films (3.01–3.1 eV) [31,53,54]. The mismatch in this case can be explained in terms of the structure of each cerium oxide (III, IV and non-stoichiometric) forming the film. However, the band gap range can be considered as an indication of the reliability of the used

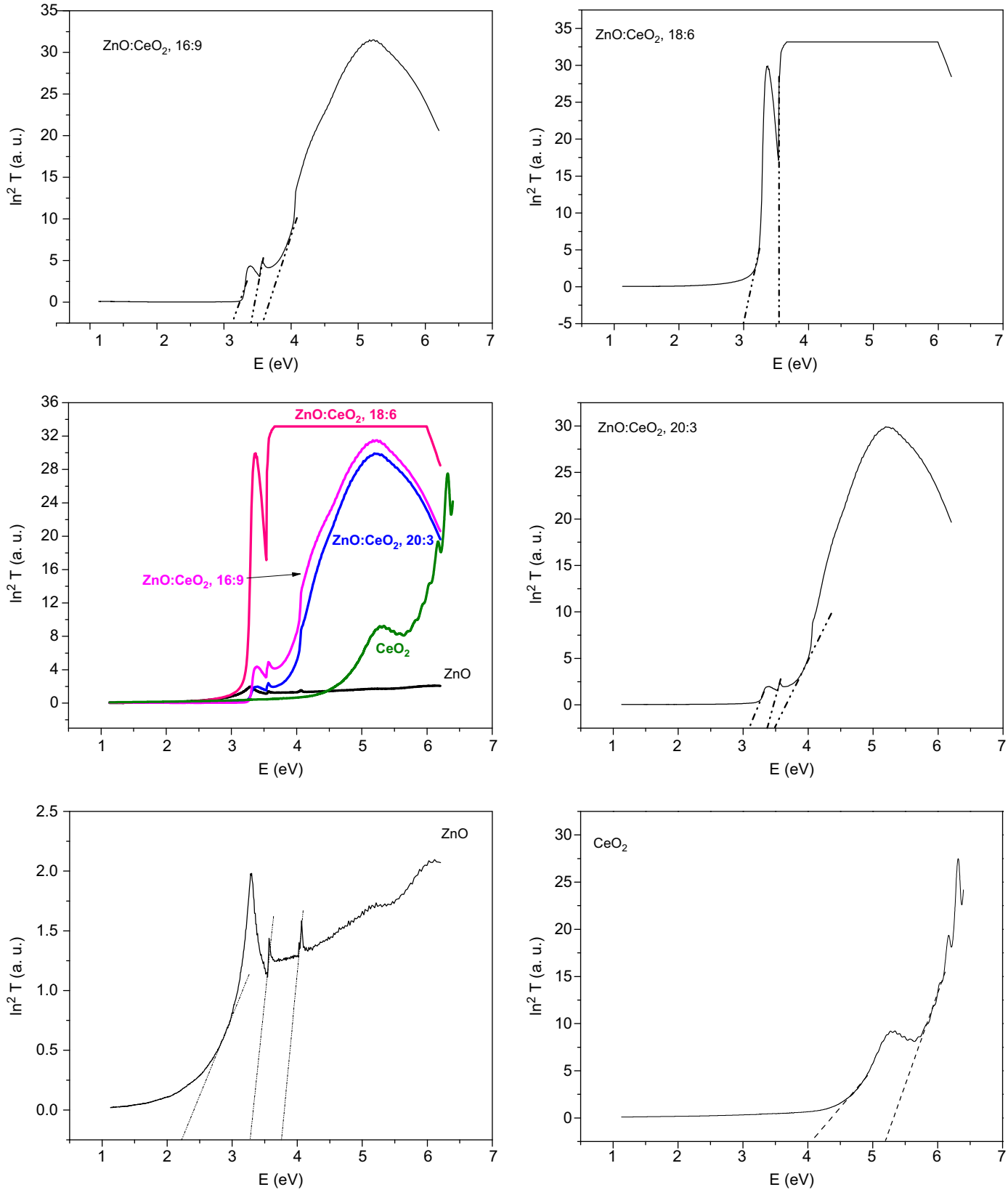

Fig. 11. Plot $\ln^2 T$ versus $h\nu$ of the as-prepared thin films and the band gap fitting.

fitting. Finally, the gap energies for $ZnO:CeO_{2-x}$ films displayed a very close band gap, although, generally it was decreased with increasing cerium contents. The reliability of the fitting is also considered in this case since no underestimation of the optical gap is found for these films. Hence, $ZnO:CeO_{2-x}$ systems present higher UV absorption and transparency in the visible region than

Table 4
Band gap from fitting.

Fitting	E_g (eV)				
	CeO_2	ZnO	ZnO–CeO_{2-x} (20:3)	ZnO–CeO_{2-x} (18:6)	ZnO–CeO_{2-x} (16:9)
1	4.06	3.75	3.57	3.54	3.47
2	5.18	3.27	3.40	3.00	3.36
3	-	2.22	3.12	–	3.08

pure oxides (ZnO and CeO_2) as a consequence of the addition of cerium to the ZnO wurzite structure. Additionally, more electrons can be contributed by cerium so that the UV region can be broader, facilitating the UV light absorption in this zone.

4. Conclusions

In this work, we have demonstrated how a simple and reproducible method can be used to control the structure and morphology of ZnO:CeO_{2-x} thin films on different amorphous and single crystalline substrates by MOCVD, using chemically stable precursors and atmospheric pressure. The ZnO:CeO_{2-x} films were successfully grown on the different substrates without carbon contamination, and film thicknesses between 2 and 2.5 μm. The structural changes of ZnO:CeO_{2-x} films depend on the excess oxygen rate or deficiency of oxygen brought into the solid solution by the donor or acceptor oxide, as well as cerium quantity. Cerium quantity also increases the tensile strain in the lattice, augmenting the surface roughness and polycrystallinity of the films. Amorphous substrates favor the formation of non-stoichiometric cerium compounds in the (400) preferential plane, where crystalline substrates induce the formation of a mixture of oxides forming polycrystalline films. Therefore, depending on orientation and growth rate, the surface morphology of the cerium content ZnO films showed different roughness: rather smooth for the (002) oriented films and much rougher when other planes appear; this phenomenon can be explained in terms of the minimization of the system total surface energy. The optimal deposition conditions displayed three dimensional structures observed for the first time for ZnO:CeO_{2-x} films. Optical studies for the as-prepared ZnO:CeO_{2-x} films in the evaluated wavelength range decreased the transparence in the visible region, but increased the absorption in the UV region. The coexistence of this remarkable structure, texture and optical properties in the same layer make these promising films very suitable for UV absorbing applications.

Acknowledgments

The authors thank R. Hernández-Reyes (IF-UNAM) for the SEM images. Financial support from Instituto Politecnico Nacional trough the SIP20100062, SIP20100087 projects; CONACYT trough the CB2006-61354 and CB2007-82314 projects; and SNI-CONACYT are gratefully acknowledged.

References

[1] Z.Y. Wu, J.H. Cai, G. Ni, Thin Solid Films 516 (2008) 7318.
[2] V.R. Shinde, T.P. Gujar, C.D. Lokhande, R.S. Mane, S.H. Han, Mater. Chem. Phys. 96 (2006) 316.
[3] J. Bao, M.A. Zimmler, F. Capasso, Nano Lett. 6 (2006) 1719.
[4] M.H. Huang, S. Mao, H. Feick, H. Yan, Y. Wu, H. Kind, E. Weber, R. Russo, P. Yang, Science 292 (2001) 1897.
[5] C.H. Ku, J.J. Wu, Nanotechnology 18 (2007) 505706.
[6] L. Liao, H.B. Lu, J.C. Li, H. He, D.F. Wang, D.J. Fu, C. Liu, W.F. Zhang, J. Phys. Chem. C 111 (2007) 1900.
[7] D.L. Marricle, T.E. Sawrr, S. Karavolis, Solid State Ionics 52 (1992) 173.
[8] Y. Xiong, K. Yamaji, N. Sakai, H. Negishi, T. Horita, H. Yokokawa, J. Electrochem. Soc. 148 (2001) E489.
[9] S. Sharma, S. Hilaire, J.M. Vohs, R.J. Gorte, H.W. Jen, J. Catal. 190 (2000) 199.
[10] S. Enzo, F. Delogu, R. Frattini, A. Primavera, A. Trovarelli, J. Mater. Res. 15 (2000) 1538.
[11] M. Ozawa, J. Alloys Compds. 275-277 (1998) 886.
[12] K. Aramaki, Corros. Sci. 48 (2006) 3298.
[13] M.F. Montemor, R. Pinto, M.G.S. Ferreira, Electrochim. Acta 54 (2009) 5179.
[14] M.E. Jouad, M.A. Lamrani, Z. Sofiani, M. Addou, T.E. Habbani, N. Fellani, K. Bahedi, L. Dghoughi, A. Monteil, B. Sahraoui, N. Gaumer, Opt. Mater. 31 (2009) 1357.
[15] J.W. Zhao, L.R. Qin, Z.D. Xiao, L.D. Zhang, Mater. Chem. Phys. 105 (2007) 194.
[16] S. Debnath, M.R. Islam, M.S.R. Khan, Bull. Mater. Sci. 30 (2007) 315.
[17] D.J. Park, J.Y. Lee, D.C. Kim, H.K. Cho, J. Phys. D: Appl. Phys. 42 (2009) 035413.
[18] L. Arurault, B. Daffos, F.X. Sauvage, Mater. Res. Bull. 43 (2008) 796.
[19] G.R. Li, D.L. Qu, L. Arurault, Y.X. Tong, J. Phys. Chem. C 113 (2009) 1235.
[20] X.J. Wang, Q.S. Lei, W. Xu, W.L. Zhou, J. Yu, Mater. Lett. 63 (2009) 1371.
[21] D. Yuravaj, K.N. Rao, K.K. Nanda, J. Phys. D: Appl. Phys. 42 (2009) 035403.
[22] H. Gómez-Pozos, A. Maldonado, M.L. de la Olvera, Mater. Lett. 61 (2007) 1460.
[23] N. Sakai., Y. Umeda, F. Mitsugi, T. Ikegami., Surf. Coat. Technol. 202 (2008) 5467.
[24] A. Mezy, G. Gerardin, D. Tichit, D. Ravot, S. Suwanboon, J.C. Tedenac, J. Ceram. Soc. Jpn. 116 (2008) 369.
[25] M.L. Addonizio, C. Diletto, Sol. Energy Mater. Sol. Cells 92 (2008) 1488.
[26] W. Park II, Metals Mater. Int. 14 (2008) 659.
[27] J. Lu, Z. Ye, J. Huang, L. Wang, B. Zhao, Appl. Surf. Sci. 207 (2003) 295.
[28] ASTM G103-97. Standar practice for preparing, cleaning and evaluating corrosion test specimens, P. A. Warrendale, USA, 2005.
[29] S.V. Samoilenkov, M.A. Stefan, G. Wahl, Surf. Coat. Technol. 192 (2005) 117.
[30] Y. Namai, K.I. Fukui, Y. Iwasawa, Catal. Today 85 (2002) 79.
[31] M. Losurdo, Thin Solid Films 455–456 (2004) 301.
[32] M. Yamashita, K. Kameyama, S. Yabe, S. Yoshida, Y. Fujishiro, T. Kawai, T. Sato, J. Mater. Sci. Lett. 37 (2002) 683.
[33] A.M. Salvi, F. Decker, F. Varsano, G. Speranza, Surf. Interf. Anal. 31 (2001) 255.
[34] A. Pfau, K.D. Schierbaum, Surf. Sci. 316 (1994) 1030.
[35] T.J.B. Holland, S.A.T. Redfern, Mineral. Mag. 61 (1997) 65.
[36] A.M. Torres-Huerta, M.A. Domínguez-Crespo, S.B. Brachetti-Sibaja, E. Ramírez-Meneses, M.A. Hernández-Pérez, ECS Trans. 25 (2009) 467.
[37] Y. Yang, M. Gao, L. Yang, Y. Zhang, J. Lang, D. Wang, Y. Wang, H. Liu, H. Fan, Appl. Surf. Sci. 255 (2008) 2646.
[38] W.J. Li, E.W. Shi, W.Z. Zhong, Z.W. Yin, J. Cryst. Growth 203 (1999) 186.
[39] Ü. Özgür, Y.I. Alivov, C. Liu, A. Teke, M.A. Reshchikov, S. Doğan, V. Avrutin, S.-J. Cho, H. Morkoç, J. Appl. Phys. 98 (2005) 041301.
[40] Z.L. Wang, Mater. Today 06 (2004) 26.
[41] H. Nörenberg, G.A.D. Briggs, Phys. Rev. Lett. 79 (1997) 4222.
[42] H. Nörenberg, G.A.D. Briggs, Surf. Sci. 424 (1999) L352.
[43] M.F. Al-Kuhaili, S.M.A. Durrani, I.A. Bakhtiari, Appl. Surf. Sci. 255 (2008) 3033.
[44] Y. Kajikawa, S. Noda, Appl. Surf. Sci. 245 (2005) 281.
[45] Y. Sun, D.J. Ryley, M.N.R. Asfhold, J. Phys. Chem. B110 (2006) 15186.
[46] X.H. Lu, G.R. Li, W.X. Zhao, Y.X. Tong, Electrochim. Acta 53 (2008) 5180.
[47] J. Yang, M. Gao, L. Yang, Y. Zhang, J. Lang, D. Wang, Y. Wang, H. Liu, H. Fan, Appl. Surf. Sci. 255 (2008) 2646.
[48] D.N.J. Lee, Mater. Sci. 34 (1999) 2575.
[49] M. Alaoui Lamrani, M. Addou, Z. Sofiani, B. Sahraoui, J. Ebotché, A. El Hichou, N. Fellahi, J.C. Bernède, R. Dounia, Opt. Commun. 277 (2007) 196.
[50] A. Becheri, M. Dürr, P. Lo Nostro, P. Baglioni, J. Nanopart. Res. 10 (2008) 679.
[51] M. Purica, E. Budianu, E. Rusu, M. Danila, R. Gavrila, Thin Solid Films 403–404 (2002) 485.
[52] M. Satoh, N. Tanaka, Y. Ueda, S. Ohshio, H. Saitoh, J. Appl. Phys. 38 (1999) L586.
[53] K.B. Sundaram, P. Wahid, Phys. Status Solidi B 161 (1990) K63.
[54] C.A. Hogarth, Z.T. Al-Dhan, Phys. Status Solidi B 137 (1986) K157.